Chemical Engineering Journal 472 (2023) 144807

Contents lists available at ScienceDirect

Chemical Engineering Journal

journal homepage: www.elsevier.com/locate/cej

Numerical simulation of surfactant-laden emulsion formation in an un-baffled stirred vessel

Fuyue Liang [a,*], Lyes Kahouadji [a], Juan Pablo Valdes [a], Seungwon Shin [b], Jalel Chergui [c], Damir Juric [c,d], Omar K. Matar [a]

[a] Department of Chemical Engineering, Imperial College London, South Kensington Campus, London SW7 2AZ, United Kingdom
[b] Department of Mechanical and System Design Engineering, Hongik University, Seoul 04066, Republic of Korea
[c] Université Paris Saclay, Centre National de la Recherche Scientifique (CNRS), Laboratoire Interdisciplinaire des Sciences du Numérique (LISN), 91400 Orsay, France
[d] Department of Applied Mathematics and Theoretical Physics, University of Cambridge, Centre for Mathematical Sciences, Wilberforce Road, Cambridge CB3 0WA, United Kingdom

ARTICLE INFO

Keywords:
Un-baffled stirred mixer
Two-phase flow
Surfactant
Mixing
LES

ABSTRACT

The present study aims to elucidate the interplay among the interfacial dynamics, surfactant transport, and underlying flow structures inside a cylindrical stirred vessel equipped with a pitched blade turbine. To address this, massively parallel three-dimensional, interface-tracking, large eddy simulations of oil-in-water dispersions are deployed to provide detailed, realistic visualisations of the intricate interfacial dynamics coupled to the turbulent flow field. In particular, we isolate the effect of surfactant arising from interfacial tension reduction and Marangoni stress (related to surfactant concentration gradient) by comparing two surfactant-laden systems, one being a realistic and experiment-achievable case, and another a simulation-exclusive system where the Marangoni stress is turned off. This comparison consists of qualitative interface visualisation as well as quantitative statistics in terms of dispersed phases counts and their size distribution. Finally, surfactant elasticity is modified with the aim of exploring its effect on the targeted mixing system.

1. Introduction

Given the heavy involvement of immiscible liquid mixing both in our daily life (e.g., food and cosmetics) and in high-end industrial applications (e.g., drug delivery), understanding the interfacial flows under highly dynamic conditions is of practical significance. Surface-active agents (surfactants) are commonly present within such systems, either by design or as contaminants, affecting both the mixing performance and the final quality of the mixed product. It is challenging to generalise the effect of surfactant in a mixing system as surfactant alters the interfacial behaviours in a complex manner that depends on surfactant distribution on the interface and its interphase transport with the bulk. In addition, the dynamic interfacial rheology (beyond the scope of this work) in such system elevates the complexity of the roles played by surfactant. Consequently, surfactant could either suppress or enhance the drop deformation under dynamic flow, affecting the mixing metrics of interest, for instance, interfacial area and equilibrium drop size distribution. These challenges hamper the understanding and control of interfacial behaviours within a surfactant-laden mixing system, which is a prevalent scenario in industry.

However, only a few studies have aimed at understanding liquid dispersion in the presence of surfactant inside a stirred vessel; most of these studies have addressed the problem regarding the surfactant influence on the final drop sizes and their distribution, leaving a gap in our understanding of the underlying physical mechanisms governing the interfacial behaviours within such system. The earliest experiment to study the effect of surfactant on drop sizes is by Lee and Soong [1] where five liquid–liquid systems and nine types of surfactants were examined. The authors found that the size of drops produced is smaller (relative to the one predicted using correlations based on clean liquid–liquid system) and more uniform (narrower drop size distribution). Later, Koshy et al. [2] developed a drop breakup model to predict the maximum drop size at various surfactant concentrations arguing that the effect of surfactant on stirred-vessel emulsification is not only by the decrease in interfacial tension, but also through the generation of an interfacial tension gradient across the interface (and thus Marangoni stress, which, albeit, was not dealt with sufficient detail in that study). Several subsequent studies have been carried out to expand knowledge in this field by considering surfactant concentration [3,4], rheological

* Corresponding author.
E-mail address: fuyue.liang18@imperial.ac.uk (F. Liang).

https://doi.org/10.1016/j.cej.2023.144807
Received 9 March 2023; Received in revised form 14 June 2023; Accepted 12 July 2023
Available online 17 July 2023

properties of surfactant-laden interface [5], and the types of surfactant head group [6]. Groeneweg et al. [7] have shown the appearance of a large number of mini-drops (a bi-modal drop size distribution) for the surfactant-laden system, and rationalised that the phenomenon is due to surfactant-induced tip-streaming [8]. More related work has been on the surfactant effect on the flow field modification in a stirred vessel; interested readers can refer to Mishra et al. [9], Arora et al. [10], Mavros et al. [11], Montante et al. [12] and references therein.

Nevertheless, interfacial dynamics on a surfactant-laden interface have been well studied by investigating drop deformation subjected to a simple flow field, both in the case of insoluble [8,13–19] and soluble surfactants [20–23], which leads to several reviews in this field (see, for example, [24,25]). More recently, Soligo et al. [26] carried out direct numerical simulations of surfactant-laden drops dispersed in turbulent flow in which a clear interplay among local flow field (considering shear stress, Marangoni stress, and the effect of Weber number), surfactant concentration and dispersed phase morphology is displayed. In their subsequent work, Soligo et al. [27] studied the flow modification introduced by the surfactant-laden drop under the same flow conditions, in terms of velocity profiles, vorticity profiles, and a specifically-defined flow topology parameter [28].

This short review of the current literature reveals the relative scarcity of information available on flow structure and interfacial dynamics in practical mixing units, such as stirred vessels, and more specifically, in the presence of surfactant. The present study attempts to elucidate the interplay among the interfacial deformation, surfactant transport, and underlying flow structure inside a cylindrical un-baffled stirred vessel equipped with a pitched blade turbine. The configuration of the vessel adapted here is partially inspired by the recent investigation performed by Busciglio et al. [29,30], where the authors showed the potential of the un-baffled stirred vessel as a viable alternative to the baffled one. This is in contrast to the view held more commonly that un-baffled stirred vessels are generally less efficient than their baffled counterparts, which led to the former being less well-studied and their flow and interfacial dynamics less explored.

The underlying physics governing the interfacial dynamics in the presence of soluble surfactant is modelled accurately thanks to a hybrid front-tracking/level-set algorithm [31], which has been extensively validated in previous studies [32–34]. Equipped with this, massively parallel, three-dimensional, large eddy simulations [35] of oil-in-water emulsification are deployed to provide detailed, realistic visualisations of the interfacial dynamics coupled to the turbulent flow field, from the onset of impeller rotation through to a state where up to 30 revolutions have completed.

The following section (Section 2) will briefly introduce the simulation technique and the governing equations. Section 3 discusses the effect of surfactant on the mixing process, decoupling the influence originating from the interfacial tension reduction and the Marangoni stress induced by the non-uniform surfactant distribution. Furthermore, we provide a parametric study of the surfactant elasticity (the sensitivity of interfacial tension to the surfactant concentration). Finally, concluding remarks, and suggestions for possible future work will be provided in Section 4.

2. Problem formulation

2.1. Simulation configuration

The configuration considered in this work is shown in Fig. 1. It consists of a cylindrical vessel of diameter $T = 8.5$ cm and height $H = 12.75$ cm, filled with water in the lower half and an overlaying oil phase above (volume fraction of oil, $\phi = 0.5$). The liquids' viscosity ratio is 5.4. The impeller employed is a pitched blade turbine (PBT), which is immersed in the water phase. Details of the impeller geometry and the physical properties of the phases are listed in Table 1.

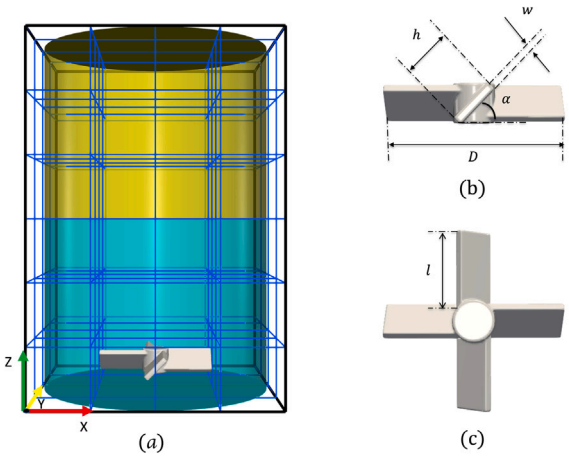

Fig. 1. (*a*) Schematic illustration of the computational domain for the oil–water mixing system: a stirred vessel, equipped with a 4-pitched-blade turbine, is filled with oil in the upper-half (coloured in gold) and water below (coloured in blue); the blades have length l, width h, and thickness w, and are inclined at an angle α to the horizontal. The computational domain is divided into $4 \times 4 \times 6$ subdomains. The number of the Cartesian structured grids per subdomain is 64^3, which gives a total grid number of $256 \times 256 \times 384$; (*b*) – (*c*) display side- and top-views of the turbine, respectively.

Table 1
Detailed geometry of the impeller and physical properties of the two phases.

Impeller geometry [cm]	
Diameter, D	4.25
Height, h	1
Thickness, w	0.2
Length, l	2.5
Clearance, C	1
Inclined angle, α [°]	45
Rotation speed, N [rps]	5
Physical properties	
Surfactant-free interfacial tension, σ_s [Pa m]	0.035
Oil viscosity, μ_o [Pa s]	5.4×10^{-3}
Water viscosity, μ_w	1.0×10^{-3}
Oil density, ρ_o [kg/m^3]	824
Water density, ρ_w	998

2.2. Governing equations

With the purpose of studying the dynamics of surfactant-laden two-phase mixing inside the stirred vessel, we solved the single-field Navier–Stokes equations in a Cartesian domain $\mathbf{x} = (x, y, z) \in [0, 8.6]^2 \times [0, 12.5]$ cm^3, as in our previous work [34] but, additionally, a varying interfacial tension is considered:

$$\nabla \cdot \bar{\mathbf{u}} = 0, \tag{1}$$

$$\rho\left(\frac{\partial \bar{\mathbf{u}}}{\partial t} + \bar{\mathbf{u}} \cdot \nabla \bar{\mathbf{u}}\right) = -\nabla \bar{p} + \nabla \cdot \left[\left(\mu + \rho C_s^2 \Delta^2 \left|\bar{S}\right|\right)\left(\nabla \bar{\mathbf{u}} + \nabla \bar{\mathbf{u}}^T\right)\right] + \rho \mathbf{g} + \mathbf{F}_{\text{fsi}} + \int_{A_e} \left[\sigma \kappa \mathbf{n} + \nabla_s \sigma\right] \delta_f(\mathbf{x} - \mathbf{x}_f)\, dA_e. \tag{2}$$

In Eq. (2), $\bar{\mathbf{u}}$ and $\bar{p}$ are respectively the ensemble-averaged velocity and pressure; $\mathbf{g}$ is the gravitational acceleration. The density, ρ, and the viscosity, μ, are given by:

$$\rho(\mathbf{x}, t) = \rho_o + \left(\rho_w - \rho_o\right) \mathbf{H}(\mathbf{x}, t),$$
$$\mu(\mathbf{x}, t) = \mu_o + \left(\mu_w - \mu_o\right) \mathbf{H}(\mathbf{x}, t),$$

where $\mathbf{H}(\mathbf{x}, t)$ represents a numerical Heaviside function, which is zero in the oil phase and unity in the water phase. The subscripts are used to indicate the corresponding liquid phases such that w is for water and

o refers to oil. In Eq. (2), C_s is the Smagorinsky-Lilly coefficient, which is fixed to the value 0.2 as it varies between 0.1–0.3 in the literature [36–40]. Next, Δ is equivalent to $V^{1/3}$ where V is the volume of a grid cell, $V = \Delta x\Delta y\Delta z$ and $|\bar{S}| = \sqrt{2\bar{S}_{ij}\bar{S}_{ij}}$ with $\bar{S}_{ij}$ being the strain rate tensor [40,41]. The term $\mathbf{F}_{\text{fsi}}$ denotes the interaction forces between impeller blades and the mixing fluids [34,42], and the last term on the right-hand-side in Eq. (2) accounts for the local interfacial force, which is decomposed into its normal component, $\sigma\kappa\mathbf{n}$, associated to the mean interface tension, and its tangential component, $\nabla_s\sigma$, the Marangoni stress; here, κ is twice the mean interface curvature, ∇_s is the surface gradient operator (i.e., $\nabla - \mathbf{n}(\mathbf{n}\cdot\nabla)$), $\mathbf{n}$ is the outward-pointing unit normal to the interface, and A_e is the normalised area of a triangular Lagrangian mesh element, e. Finally, $\mathbf{x}_f$ is a parameterisation of the interface, and $\delta_f\left(\mathbf{x}-\mathbf{x}_f\right)$ is a Dirac distribution that is non-zero only when $\mathbf{x}=\mathbf{x}_f$.

In the present work, surfactant is soluble in the bulk (the continuous phase), such that surfactant transport is resolved both in the bulk and on the interface. The interfacial concentration, Γ, is governed by:

$$\frac{\partial\Gamma}{\partial t} + \nabla_s\cdot(\Gamma\mathbf{u}_t) = D_s\nabla_s^2\Gamma + J. \tag{3}$$

More specifically, the left-hand-side terms represent the transient transport and the convection caused by the bulk flow, respectively, where $\mathbf{u}_t$ is the tangential velocity vector on the interface, which is computed from the interface velocity, $\mathbf{u}_s$, via $\mathbf{u}_t = \left(\mathbf{u}_s\cdot\mathbf{t}\right)\mathbf{t}$, with $\mathbf{t}$ being the unit vector tangential to the interface. The first term on the right corresponds to interface diffusion, and D_s is the surfactant diffusivity in the plane of the interface; J accounts for the mass flux from the bulk. In general, the flux from the bulk is determined by surfactant adsorption which can be divided into two time-dependent processes: the diffusion of surfactant from the bulk phase (diffusion flux, J_{diff}) and the adsorption onto the interface (adsorption/desorption flux, $J_{\text{a/d}}$). Firstly, $J_{\text{a/d}}$ can be written as:

$$J_{\text{a/d}} = k_a C_{\text{sub}}(\Gamma_\infty - \Gamma) - k_d\Gamma, \tag{4}$$

where k_a and k_d are the kinetic coefficients for adsorption and desorption, respectively, and Γ_∞ is the saturation concentration on the interface; C_{sub} represents the surfactant bulk concentration evaluated at the layer immediately adjacent to the interface, which is known as the bulk "sub-phase". This sub-phase concentration is determined by diffusion from the bulk:

$$J_{\text{diff}} = -D_b\mathbf{n}\cdot\nabla C|_{\text{sub}}, \tag{5}$$

where D_b refers to the diffusivity in the bulk phase, and C is the surfactant concentration in the bulk which is governed by the convection–diffusion equation as follows:

$$\frac{\partial C}{\partial t} + \mathbf{u}\cdot\nabla C = D_b\nabla^2 C. \tag{6}$$

To satisfy conservation of surfactant, the diffusive flux from the bulk, Eq. (5), balances the kinetic sorptive flux, Eq. (4), and both mechanisms govern the flux to the interface [21,43]. Hence,

$$J = J_{\text{a/d}} = J_{\text{diff}}. \tag{7}$$

When surfactant adsorbs onto the interface, the interfacial tension decreases from its clean surface value, σ_s. The Langmuir relation is used herein to describe such an effect:

$$\sigma = \sigma_s + \mathcal{R}T\Gamma_\infty\ln\left(1-\frac{\Gamma}{\Gamma_\infty}\right) = \sigma_s\left[1+\beta_s\ln\left(1-\frac{\Gamma}{\Gamma_\infty}\right)\right], \tag{8}$$

Herein, $\mathcal{R}$ denotes the ideal gas constant, T the temperature, and the dimensionless parameter β_s is defined as surfactant elasticity, which measures the sensitivity of the interfacial tension to the surfactant concentration. This equation describes the fact that the interfacial tension drops steeply as the surfactant concentration approaches unity from below [44]. However, this relation could predict unrealistic behaviours namely that the interfacial tension becomes negative for finite value of Γ. To avoid this, the relation is modified as follows:

$$\sigma/\sigma_s = \max\left[0.05, 1+\beta_s\ln\left(1-\frac{\Gamma}{\Gamma_\infty}\right)\right]. \tag{9}$$

The governing equations are recast in dimensionless form according to the following scaling:

$$\begin{aligned}
&\tilde{\mathbf{x}} = \frac{\mathbf{x}}{D}, \quad \tilde{t} = \frac{t}{1/N}, \quad \tilde{\mathbf{u}} = \frac{\bar{\mathbf{u}}}{ND}, \quad \tilde{\mathbf{g}} = \frac{\mathbf{g}}{g},\\
&\tilde{p} = \frac{\bar{p}}{\rho_w(ND)^2}, \quad \tilde{\mu} = \frac{\mu}{\mu_w}, \quad \tilde{\rho} = \frac{\rho}{\rho_w},\\
&\tilde{\sigma} = \frac{\sigma}{\sigma_s}, \quad \tilde{\Gamma} = \frac{\Gamma}{\Gamma_\infty}, \quad \tilde{C} = \frac{C}{C_0}, \quad \tilde{C}_{\text{sub}} = \frac{C_{\text{sub}}}{C_0},
\end{aligned} \tag{10}$$

where the tildes indicate the dimensionless quantities. Here, space $\mathbf{x}$ and time t are made non-dimensional by the impeller diameter, D, and the duration for one impeller revolution, $1/N$, respectively. Hence, the velocity and pressure are scaled using the impeller velocity, ND, and $\rho_w(ND)^2$, respectively. Moreover, C_0 denotes the initial surfactant concentration in the bulk. On this basis, the governing equations become:

$$\nabla\cdot\tilde{\mathbf{u}} = 0, \tag{11}$$

$$\begin{aligned}
&\tilde{\rho}\left(\frac{\partial\tilde{\mathbf{u}}}{\partial\tilde{t}} + \tilde{\mathbf{u}}\cdot\nabla\tilde{\mathbf{u}}\right) + \nabla\tilde{p} = \frac{1}{\text{Re}}\nabla\cdot\tilde{\mu}\left(\nabla\tilde{\mathbf{u}} + \nabla\tilde{\mathbf{u}}^T\right)\\
&-\nabla\cdot\left(\tilde{\rho}2C_s^2\tilde{\Delta}^2\left|\tilde{S}\right|\right)\left(\nabla\tilde{\mathbf{u}} + \nabla\tilde{\mathbf{u}}^T\right) + \frac{1}{\text{Fr}}\tilde{\rho}\tilde{\mathbf{g}} + \tilde{\mathbf{F}}_{\text{fsi}}\\
&+\frac{1}{\text{We}}\left(\int_{\tilde{A}_e}\left(\tilde{\sigma}\tilde{\kappa}\mathbf{n} + \nabla_s\tilde{\sigma}\right)\delta_f(\tilde{\mathbf{x}}-\tilde{\mathbf{x}}_f)\,d\tilde{A}_e\right).
\end{aligned} \tag{12}$$

$$\frac{\partial\tilde{\Gamma}}{\partial\tilde{t}} + \nabla_s\cdot\left(\tilde{\Gamma}\tilde{\mathbf{u}}_t\right) = \frac{1}{\text{Pe}_s}\nabla_s^2\tilde{\Gamma} + \tilde{J}, \tag{13}$$

$$\tilde{J}_{a/d} = \text{Bi}\left[k\tilde{C}_{\text{sub}}(1-\tilde{\Gamma}) - \tilde{\Gamma}\right], \tag{14}$$

$$\tilde{J}_{\text{diff}} = -\frac{1}{\text{Pe}_b h}\mathbf{n}\cdot\nabla\tilde{C}|_{\text{sub}} \tag{15}$$

$$\frac{\partial\tilde{C}}{\partial\tilde{t}} + \tilde{\mathbf{u}}\cdot\nabla\tilde{C} = \frac{1}{\text{Pe}_b}\nabla^2\tilde{C}, \tag{16}$$

$$\tilde{\sigma} = \max\left[0.05,\ 1+\beta_s\ln\left(1-\tilde{\Gamma}\right)\right]. \tag{17}$$

In these equations, the dimensionless parameters are defined as follows:

$$\begin{aligned}
&\text{Re} = \frac{\rho_w N D^2}{\mu_w}, \quad \text{Fr} = \frac{N^2 D}{g}, \quad \text{We} = \frac{\rho_w N^2 D^3}{\sigma_s},\\
&\text{Pe}_b = \frac{ND^2}{D_b}, \quad \text{Pe}_s = \frac{ND^2}{D_s}, \quad \text{Bi} = \frac{k_d}{N},\\
&h = \frac{\Gamma_\infty}{DC_0}, \quad k = \frac{k_a C_0}{k_d}, \quad \beta_s = \frac{\mathcal{R}T\Gamma_\infty}{\sigma_s}.
\end{aligned} \tag{18}$$

Re, Fr and We are the Reynolds number (ratio of inertial to viscous forces), Froude number (ratio of inertial to gravitational force) and Weber number (ratio of inertial forces to interfacial tension), respectively. Pe_b and Pe_s are the bulk and interfacial Peclét numbers, separately providing the relative significance of convection and diffusion in the bulk and on the interface. The Biot number, Bi, expresses the ratio of characteristic desorptive to convective speed on the interface; h stands for the adsorption depth that characterises the diluted region beneath the interface caused by adsorption; k is the adsorption parameter, which represents the ratio of adsorption coefficient, k_a, to desorption coefficient, k_d. All these parameters are well known in literature [32,33,45–48]. For simplicity, the tildes that designate dimensionless quantities are dropped henceforth. Finally, the dimensionless timescale we use in the following discussion, in the form of $t = n\times Rev.$, refers to the instant when n impeller revolutions are completed.

To achieve high-fidelity simulations regarding the dynamic interface and its interfacial tension forces, we use a hybrid front tracking/level-set technique, which is known as the Level Contour Reconstruction

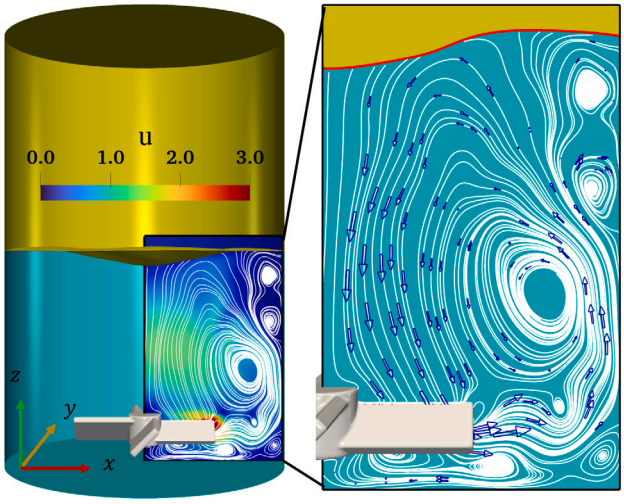

Fig. 2. Flow field prior to the interface deformation ($t = 8 \times Rev.$) for a surfactant-free system, represented by streamlines drawn on a $x - z$ plane at $y = 4.3$ cm. The inset of the three-dimensional vessel is coloured by the velocity magnitude, and the blue arrows shown in the close-up view (representing velocity orientations) are scaled by the velocity magnitude.

Method (LCRM) [31], where surfactant transport and interfacial stresses shown above are fully resolved. Adaptive time steps are applied in our temporal discretisation process, which is based on second-order GEAR method, and the time-step value Δt is carefully chosen at each temporal iteration in order to satisfy a robust numerical stability via a criterion based on:

$$\Delta t \leq \min\left\{\Delta t_{\text{cap}}, \Delta t_{\text{vis}}, \Delta t_{\text{CFL}}, \Delta t_{\text{int}}, \Delta t_{\text{surf}}\right\} \tag{19}$$

where Δt_{cap}, Δt_{vis}, Δt_{CFL}, Δt_{int}, and Δt_{surf} represent the capillary, viscous, Courant–Friedrichs–Lewy (CFL), interfacial CFL, and surfactant time-steps, respectively, defined by:

$$\Delta t_{\text{cap}} \equiv \frac{1}{2}\left(\frac{\left(\rho_o + \rho_w\right)\Delta x_{\min}^3}{\pi\sigma}\right)^{1/2},$$

$$\Delta t_{\text{vis}} \equiv \min\left(\frac{\rho_w}{\mu_w}, \frac{\rho_o}{\mu_o}\right)\frac{\Delta x_{\min}^2}{6},$$

$$\Delta t_{\text{CFL}} \equiv \min_j\left(\min_{\text{domain}}\left(\frac{\Delta x_j}{\|u_j\|}\right)\right),$$

$$\Delta t_{\text{int}} \equiv \min_j\left(\min_{\tilde{A}_e(t)}\left(\frac{\Delta x_j}{\|U\|}\right)\right),$$

$$\Delta t_{\text{surf}} \equiv \frac{\Delta x_{\min}^2}{6D_b},$$

where $\Delta x_{\min} = \min_j(\Delta x_j)$ refers to the minimum size x at a given cell j; u_j, and U are the maximum fluid and interface velocities, respectively.

In addition, the Direct Forcing Method used by Mohd-Yusof [49] and Fadlun et al. [50] is applied to incorporate the complex geometry of the impeller and its rotation. More information on the numerical technique applied to computation and related validations can be found in [34,42,51].

2.3. Parameter values adopted in simulations

In our previous work [34], we investigated the interface evolution under a range of impeller speeds (N = 1–10 rps, Re = 1802–18 026). Herein, we fixed the impeller speed to $N = 5$ rps, since our concern is currently on the effect of surfactant. This gives values of Re = 9013, We = 55, and Fr = 0.1. The large Weber number which characterises our flow indicates the heavy dominance of inertial forces in the system; in addition, as we will present in the next section, complex interacting structures (or vortices) are generated (see Fig. 2). Hence, the studied system, especially the region near the impeller, is treated as turbulent, where the physics we extract is therefore generic to turbulent oil–water emulsification in stirred vessels.

To investigate the surfactant effect, we set up a "base" surfactant-laden case with surfactant-related parameters fixed to $C_0 = 4 \times 10^{-4}$ mol m^{-3}, $k_a = 6.68 \times 10^4$ m^3 mol^{-1} s^{-1}, $k_d = 3.14$ s^{-1}, and $\Gamma_\infty = 1 \times 10^{-5}$ mol m^{-2}. In particular, C_0 is calculated via $C_0 = \Gamma_\infty / R$, where R is the radius of the impeller, as a reference bulk concentration, which is also chosen as its initial value. Typical values for the surfactant adsorption and desorption coefficients, k_a and k_d, are quoted from relevant reviews provided in [52–54], where k_d is claimed to be within the range of $O(10^{-4}) < k_d \left[\text{s}^{-1}\right] < O(10^2)$ depending on the chemical structure of the surfactant molecules, while k_a is in the range $O(10^{-1}) < k_a \left[\text{m}^3\ \text{mol}^{-1}\ \text{s}^{-1}\right] < O(10^6)$. In our base case, k_a and k_d are selected as the listed values exploring the scenario where the surfactant is inclined to absorb onto the interface, with a ratio of adsorption to desorption $k = k_a C_0 / k_d \approx 10$. In this limit, combined with the value of Bi determined via k_d / N (= $O(10^{-1})$ indicating a fast convection driven by ambient flow in comparison to surfactant desorption), the adsorbed surfactant can approximately perform as an insoluble layer. In addition, the maximum packing concentration at the interface is set to $\Gamma_\infty \approx O(10^{-5})$ mol m^{-2}, as the same order of magnitude reported in experimental results for the surfactant such as Sodium Dodecyl Sulphate (SDS) [44,55]. This gives the values of $\beta_s \approx 0.7$ computed using the room temperature, $T = 298.15$ K, and $h \approx 0.5$. An upper and lower limit of β_s, in addition to the base case, are investigated to recover the effect of surfactant sensitivity (i.e., $\beta_s = 0.5, 0.7, 0.9$).

We also fix both Peclét numbers in the bulk and on the interface as $Pe_b = Pe_s = 4.6 \times 10^2$. This comes from the recent remarks from [32,33,56] stating that negligible effect arises from Pe_s when it is increased further above 10^2; moreover, Pe_b is kept equal to Pe_s as suggested in [32], which also follows the guideline given by Ratulowski and Chang [57] to achieve a balance between adsorption and interfacial convection, assuring both convective and diffusive transport are resolved in the simulated system.

Finally, as mentioned previously, a second effect from surfactant arises from the Marangoni stress, which is induced due to the surfactant concentration gradient and hence can be computed via Γ:

$$\tau \equiv \nabla_s \sigma \cdot \mathbf{t} = -\frac{\beta_s}{1 - \Gamma}\left(\mathbf{t} \cdot \nabla_s \Gamma\right). \tag{20}$$

To isolate this effect from that induced by the interfacial tension reduction, another surfactant-laden case is set up where the Marangoni stress is turned off by eliminating the term $\nabla_s \tilde{\sigma}$ from Eq. (2). This additional case allows us to unequivocally elucidate the mechanisms by which the interfacial tension reduction and surfactant concentration gradient act in tandem to modify the surfactant-free interface dynamics.

3. Results and discussion

In this section, we present a discussion of our results, starting with a comparison of the current predictions against our previous work where we studied the flow profiles and interfacial dynamics inside a surfactant-free agitated vessel (with an identical configuration) [34]. Using qualitative visualisation and quantitative statistics (i.e., time evolution of dispersed entity number and drop size distribution at the instant where the simulation is terminated), the comparison provides an insight into how the presence of surfactant modifies the liquid dispersion process in the studied system. We then demonstrate the effect of surfactant elasticity (β_s) via a parametric study.

The results associated with the surfactant-free system have been validated against the experimental work done by Hančil and Rod [58] where single drop breakage in a stirred vessel was investigated. In addition, a grid independence test has been carried out to confirm that the mesh size we used is sufficient to provide reliable predictions of 'real'

liquid–liquid mixing. Regarding the surfactant transport in multiphase systems, Shin et al. [31] have performed comprehensive benchmark tests of the numerical procedure employed in the present study against analytical results, which involve surfactant diffusion on the interface and in the bulk. For the current study, we also performed a validation study against a recent experimental investigation on drop size in an oil–water dispersion [59]. Information related to the two experimental validations can be found in the Supplementary Information section.

3.1. Surfactant-free system from previous work

Prior to the discussion of the roles played by the surfactant, the flow field generated in the current configuration, and surfactant-free interface evolution are briefly considered. Generally, as presented in Fig. 2, the impeller pumps the flow radially outward (analogous to the von Kármán flow over a infinite rotating disc [60]). The no-slip fixed vessel wall modifies this flow, along which the flow develops upward to the interface. After this, the flow is dragged to the vessel centre by a centrifugal force at the interface. Finally, a strong elongational flow is presented at the vessel centre, which indicates a large tendency for the fluid to travel down back to the impeller, giving rise to flow circulation. Such process generates a myriad of vortical structures and therefore a flow field of high complexity where different mechanisms govern the drop deformation depending on the local flow type [61].

Following the flow field described, the liquid dispersion in the studied configuration is achieved by following several steps: (1) *interface deformation:* the rotating impeller deforms the flat interface downward in a swirling motion until both contact; (2) *ligament formation:* the impeller shear cuts off the deforming interface giving birth to ligament(s); (3) *drop breakup:* the ligament elongates until it breaks into multiple individual drops via a capillary instability (see Fig. 6, and detailed mechanism has been described in [62] as "transient dispersion" or "capillary breakup"). Likewise, this breakup mechanism is analogous to the "end-pinching" phenomenon described in [63], which refers to the breakup of an elongated drop after a sudden halt of the flow rate, where the flow rate interruption corresponds to the inherently periodic velocity field [64–66] introduced by the impeller rotation herein. Particularly for the current impeller speed, there exits a retraction of the deforming interface (due to the interfacial tension competing against the elongational flow), which leads to (4) *the cessation of interface-impeller contact* and no further ligaments being produced. Meanwhile, the dispersed entities are likely to travel up to the overlying oil phase given the underlying flow field, and in addition, due to buoyancy.

3.2. Surfactant effect on interface evolution

In this part, we compare three cases with regard to the interface evolution described above including (1) surfactant-free system from our previous work, (2) surfactant-laden I ($|\tau| > 0$), and (3) surfactant-laden II with Marangoni stress turned off ($|\tau| = 0$).

3.2.1. Step 1: Interface deformation

Fig. 3 presents the interfacial shapes at early times ($t = 8.5 - 12 \times Rev.$) for the three cases, where the interface begins to deviate from its flat position, and a few dispersed entities are formed. The first observation that can be drawn from the figure is that the deformation of the surfactant-laden interface (I) is accelerated in comparison to its surfactant-free counterpart (see Fig. 3-(a)–(b) and -(f)–(g)). This is expected since the presence of surfactant reduces the average interfacial tension, and therefore, promotes the interface deformation under the same flow condition.

However, Fig. 3-(c) and -(h) show that the deforming interfaces for the two cases subsequently reach similar positions (relative height in the vessel). To better illuminate the observation, Fig. 4-(a) depicts the deformation by plotting the temporal evolution, in terms of the minimum position of the interface and the corresponding axial component of interfacial velocity at that location (as schematically shown in Fig. 3-(a)). The position refers to the relative height in the cylindrical vessel which is scaled using the height of vessel, $\tilde{z} = (2z - H)/H$, and only the magnitude of velocity is plotted as $|u_z|$, since it always points downward during this step. This plot shows that while the interface approaches the impeller (decreasing $\tilde{z}$), $|u_z|$ increases to a peak value and then a reduction is seen. A similar conclusion as above, that the accelerated deformation is associated with the surfactant-laden interface (I), can be made prior to the velocity peak. It is also evident that the subsequent decrease in $|u_z|$ is more significant for the surfactant-laden case I. This can be explained by the fact that surfactant on the deforming interface is accumulated at its minimum position (i.e., the descending leading edge of the interface), which introduces an opposing Marangoni stress pointing upward. Fig. 4-(b) exemplifies the surfactant distribution on the interface at $t = 9 \times Rev.$. As shown, the induced Marangoni stress, which opposes the downward flow at the vessel centre, acts to decelerate the interface deformation. A possible explanation to the overall acceleration prior to the velocity peak can be the dominance of the inertia, namely the strong downward flow where the retraction driven by the Marangoni stress is negligible. After that, the interface reaches the vicinity of the impeller, at which the flow field starts to develop radially, and therefore, the vertical deformation of interface slows down. Thus, the retarding effect of the Marangoni stress [8,56] commences to function, causing the further decrease in $|u_z|$ seen for the surfactant-laden case I. This process of deformation is clearly described via $\tilde{z}$ in Fig. 4-(a) that, at $t = 10 \times Rev.$, the surfactant-laden interface (I) reaches the same height in the vessel as the surfactant-free interface after the acceleration and the subsequent deceleration.

Moreover, the effect of Marangoni stress demonstrated above can be better appreciated via the surfactant-laden system II. The visualisation of the Marangoni-free interface indicates that Marangoni stress plays a role in retaining the plump and thick shape of the deforming interface, as well as the relatively uniform surfactant concentration over the interface. The evidence can be seen in Fig. 3-(k), which indicates that the Marangoni-free interface is in a slender shape with varying interfacial surfactant concentration, as opposed to what is shown for the surfactant-laden system in the presence of Marangoni stress. Additionally, from Fig. 4-(a), decelerating deformation occurs for the Marangoni-free system while the interface is near the impeller. However, the "braking" (i.e., $|u_z| \to 0$ and the negligible change in $\tilde{z}$) observed for the other two cases no longer takes place, which provides additional support to the previous statement that Marangoni stress leads to further deceleration of interface deformation in addition to that which arises due to the radially-developing flow field.

Another interesting phenomenon is the formation of the "branches" at the surfactant-laden interface (I) (see Fig. 3-(i)). Such phenomenon can be related to the fact that given the underlying flow described previously, where the flow develops towards the vessel wall, ligaments are prone to be formed elongating radially behind the impeller hub. Furthermore, this can be better demonstrated using the flow topology parameter, Q, which was first used in [28] and recently became popular in the field of multiphase flows [27]. This parameter helps distinguish among the three types of flow topology locally and is computed using the rate-of-deformation, $\boldsymbol{D}$, and rate-of-rotation tensors, $\boldsymbol{\Omega}$:

$$Q = \frac{\boldsymbol{D}^2 - \boldsymbol{\Omega}^2}{\boldsymbol{D}^2 + \boldsymbol{\Omega}^2} \begin{cases} = -1, & \text{for rotational flow} \\ = 0, & \text{for shear flow} \\ = +1, & \text{for elongational flow,} \end{cases} \tag{21}$$

where $\boldsymbol{D}^2 = \boldsymbol{D} : \boldsymbol{D}$ and $\boldsymbol{\Omega}^2 = \boldsymbol{\Omega} : \boldsymbol{\Omega}$; $\boldsymbol{D}$ and $\boldsymbol{\Omega}$ can be calculated from the velocity gradient tensor $\nabla \mathbf{u}$:

$$\boldsymbol{D} = \frac{\nabla \mathbf{u} + \nabla \mathbf{u}^T}{2},$$
$$\boldsymbol{\Omega} = \frac{\nabla \mathbf{u} - \nabla \mathbf{u}^T}{2}.$$

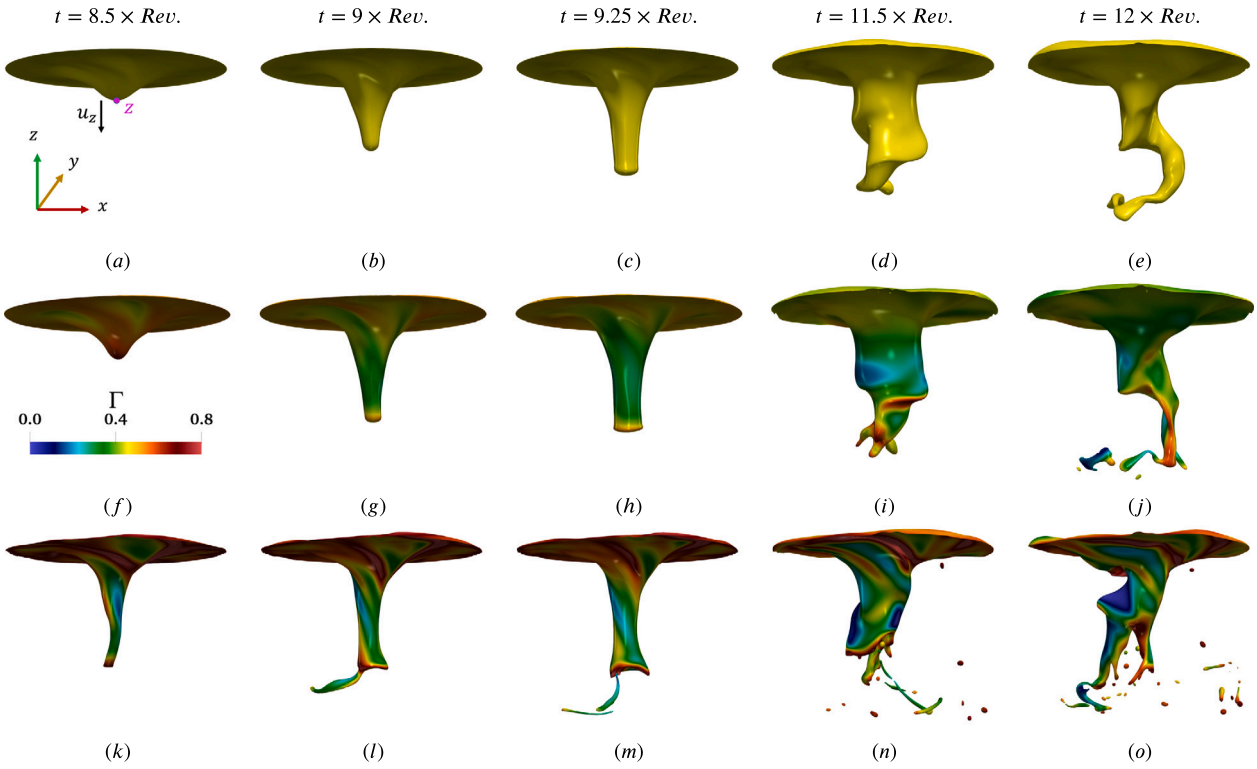

Fig. 3. Comparative evolution of interfacial shapes for the surfactant-free (top), surfactant-laden I ($|\tau| > 0$, middle) and surfactant-laden II ($|\tau| = 0$, bottom) systems for $t = 8.5 - 12 \times Rev$. The interface is coloured by the magnitude of Γ. The values of surfactant-related parameters correspond to the "base" case (see Section 2.3).

Fig. 5 compares the probability density function (P.D.F.) of parameter Q at the surfactant-free and surfactant-laden interfaces (I) at $t = 11.5 \times Rev.$, corresponding to Fig. 3-(d) and -(i), respectively. In this case, the statistics are only computed at the interface, which exclude the effect of internal and external flow enabling us to isolate the flow modification induced by the interfacial tension reduction. Nevertheless, albeit not presented herein, negligible difference is observed in terms of the internal and external flow types for both systems (dominated by the pure shear flows), which indicates that the flow modification is mainly at the interface. As can be seen from Fig. 5, for a surfactant-covered interface (I), there is a decreasing possibility of seeing elongation-dominated flow, while a larger probability to experience shear-like flow is observed. This could be a possible explanation for "branch" formation as the deforming interface is more likely to be torn apart, rather than being stretched, under the modified flow topology. Consequently, these "branches" give way to ligament development accompanied by dispersed drop production via a surfactant-induced tip-streaming mechanism (more discussion in the following Section 3.2.2). In contrast, as shown in Fig. 3-(e), the surfactant-free interface keeps elongating and thinning, following a helical trajectory due to the impeller rotation, until the first ligament is formed ($\approx 12.375 \times Rev.$, which is not presented in the figure).

For the Marangoni-free system, a sequence of thin ligaments are produced at the minimum position of the interface (Fig. 3-(l), (m)), quickly followed by the formation of highly surfactant-concentrated drops (Fig. 3-(n), (o)), all of which is a consequence of the plummeting interfacial tension that takes place in regions with surfactant surplus. These observations, once again, reflect the fact that Marangoni stress is activated to avoid surfactant from accumulating in excess at the minimum position of the interface. The absence of this phenomenon is directly responsible for the "free" escape and detachment of ligaments from the deforming interface, as seen in Fig. 3-(m), (n).

3.2.2. Steps 2&3: Ligament and drop formation

As indicated earlier, during Steps 2 and 3, a large amount of dispersed entities is produced via distinct mechanisms. In our previous work, we suggested that following the ligament generation, dispersed drops in the surfactant-free system are formed via a capillary instability (see Fig. 6), where one elongated ligament gives birth to multiple individual drops. For the surfactant-laden system I, an additional drop breakup mechanism is promoted, namely tip- streaming/dropping [7, 8]. Fig. 6 displays the close-up visualisations of various drop breakup events observed in the surfactant-free and surfactant-laden I systems (during $t = 12 - 18 \times Rev.$), exemplifying those via capillary instability and tip-streaming. For the former mechanism, two examples from different systems are presented, whereas two scenarios for surfactant-induced tip-streaming are extracted from the surfactant-laden system I. The first tip streaming is initiated from the deforming interface, which leads to an individual drop formation prior to long ligament formation, in contrast to what we observed from the surfactant-free system (see Section 3.1). This can be an influencing factor on the transient dispersed entities number profile (more details are deferred to Section 3.3.1). Likewise, in the second case, where the breakup is from an elongated ligament, tip-streaming generates drops intermittently, leaving a large and relatively clean (i.e., covered by less surfactant) drop after emission of several daughter drops.

An interesting feature for the Marangoni-free case is that drop breakup via capillary instability is suppressed, and dispersed drops are formed via either binary breakup from larger drops or tip-streaming from stretching ligaments. Fig. 7-(a) illustrates the effect of Marangoni stresses on the stretching ligament prior to its breakup via capillary instability (using the example shown in Fig. 6). As presented, Marangoni stresses play different roles on each end of the ligament depending on the local surfactant distribution. First, for the ligament pole labelled as A, surfactant is accumulated at the bulbous end, which introduces a Marangoni stress towards the ligament body, impeding the formation of an individual drop. On the other hand, surfactant concentration at the pole B is lower relative to the nodule region, giving rise to a Marangoni stress pointing outward and thus enhancing the ligament elongation. From this perspective, Marangoni stress encourages the commencement of breakup events driven by capillary instability by facilitating the

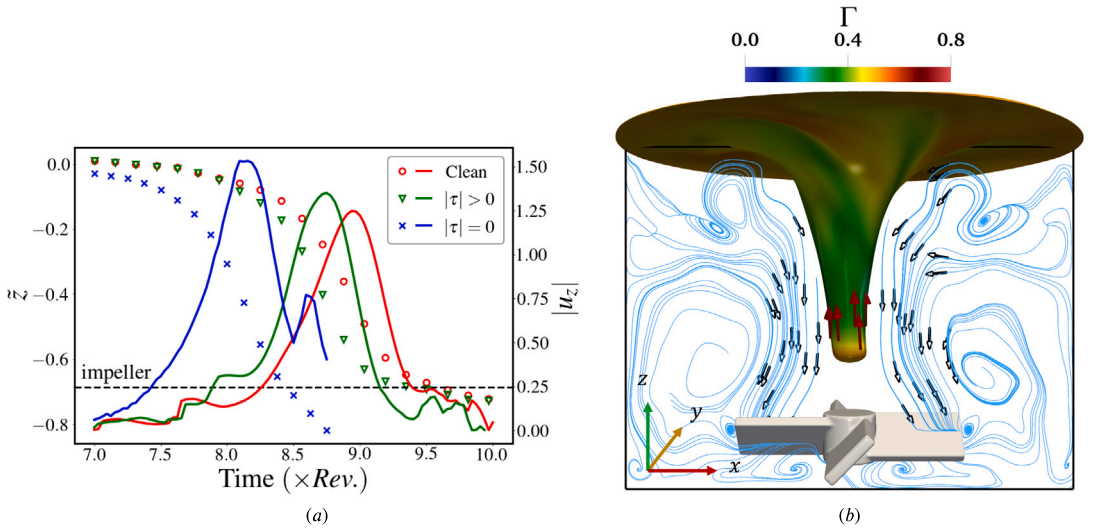

Fig. 4. (*a*) Temporal evolution of the interfacial deformation for the three studied cases for $t = 7 - 10 \times Rev.$ with regard to the minimum position of the deforming interface ($\tilde{z}$ shown by symbols) and the magnitude of the velocity of the vertical interface deformation ($|u_z|$ shown by lines); (*b*) the interplay between the flow field (streamlines in blue along with black arrows representing their directions) at the vessel centre and the induced Marangoni stresses (red arrows) at the deforming interface for $t = 9 \times Rev.$. The interface is coloured by the magnitude of Γ. The surfactant-related parameter values remain unchanged from Fig. 3.

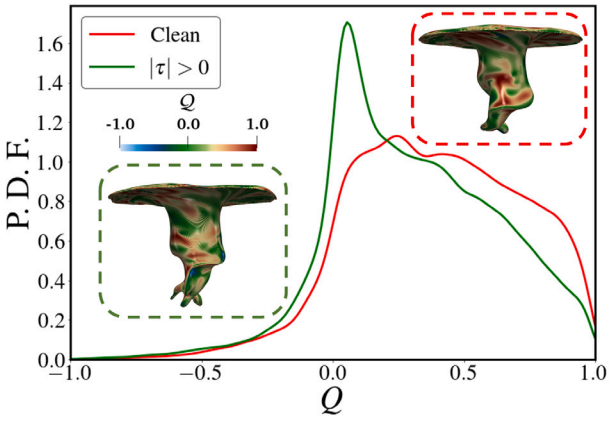

Fig. 5. Probability density function of parameter Q for surfactant-free and surfactant-laden I interfaces at $t = 11.5 \times Rev.$. The interfaces are coloured by Q. The surfactant-related parameters are the same as in Fig. 3.

ligament's stretching motion and inhibiting drops from bursting at the poles. This effect, combined with the promotion of tip-streaming, leads to the observation that both mechanisms exist in the surfactant-laden system I.

Nevertheless, in the case of drop deformation, it is common to see the same surfactant distribution profile as in the pole *A*, since surfactant tends to be swept towards the poles. As stated in the discussion related to Step 1, Marangoni stress acts as a stabilising factor against drop deformation, either delaying or even avoiding the new drop production in this step. Fig. 7-(*b*) provides evidence of this by comparing the behaviour of one drop located in the vicinity of the impeller at $t = 15.5\times Rev.$ for both surfactant-laden systems ($|\tau| = 0$ and $|\tau| > 0$ shown at the top and bottom of the figure, respectively). The critical Weber number for drop breakup has been reported for various types of flows, which consistently lies in the range of $O(10^1)$, for instance, $We_{crit} \approx 1$ for turbulent emulsification [67,68], $We_{crit} \approx 3 - 7$ in the cases of uniaxial shear and elongation flow [69] and nonuniform shear [70]. Based on this, both drops are likely to break given their sizes ($D_{d,|\tau|>0} = 0.53$ cm and $D_{d,|\tau|=0} = 0.40$ cm, obtained as the corresponding sphere diameter of its interfacial area) and their local Weber numbers ($We_{|\tau|>0} = 103.6$ and $We_{|\tau|=0} = 93.2$, calculated with the impeller tip velocity and average interfacial tension at the interface). However, it is evident that the drop with Marangoni stress turned on retracts to its spherical shape rather than the predicted drop fragmentation according to We_{crit}. This is attributed to, as shown in the figure inset, the existence of Marangoni stress pointing from drop poles to drop equator. This comparison strengthens what has been demonstrated previously that Marangoni stress hinders elongation and induces the retraction of the drop back to its spherical shape. Furthermore, the presence of Marangoni stress reduces the deformability of the deforming interface making it more rigid as shown in Fig. 7-(*c*). From the figure, surfactant is accumulated at the stretching tip of the deforming interface and is less concentrated at the belly, which establishes a surfactant concentration gradient. Consequently, the induced Marangoni stress immobilises the interface preventing it from deforming into multiple branches (as shown for the Marangoni-free case), which is inclined to generate dispersed drops freely.

3.2.3. Step 4: Cessation of interface-impeller contact

As mentioned previously, the deforming interface retracts upward at $t = 20\times Rev.$, leading to the cessation of interface-impeller contact thereafter. Fig. 8-(*a*) exemplifies the interfacial behaviours for the three cases at $t = 25\times Rev.$. As shown, the interface remains in a generally concave shape, which shows some resemblance to the well-known "Newton's Bucket" flow generated in a rotating cylinder [71–73], or the air–water surface deflection in the shape of an inverted bell observed in rotating flows [74]. Herein, given the current impeller speed, the surfactant-free interface rotates following the impeller motion and no further ligaments are generated. In contrast, intermittent ligament formation is seen for the two surfactant-laden systems despite the cessation of interface-impeller contact. This is presumably caused by the surfactant accumulation at the minimum position of the interface which decreases the interfacial tension that would otherwise have counteracted ligament formation. In addition, the visualisation of interface in the presence of Marangoni stress highlights its increased rigidity (circled in orange in Fig. 8-(*a*)) relative to its Marangoni-free counterpart, which indicates again the immobilising effect of the Marangoni stress against interfacial deformation.

It is also worth noting that the dispersed drop tends to either coalesce with one another or merge back with the "inverted bell". Each case leads to different outcomes, as exemplified by the interfacial evolution in the case of surfactant-laden system I, as displayed in

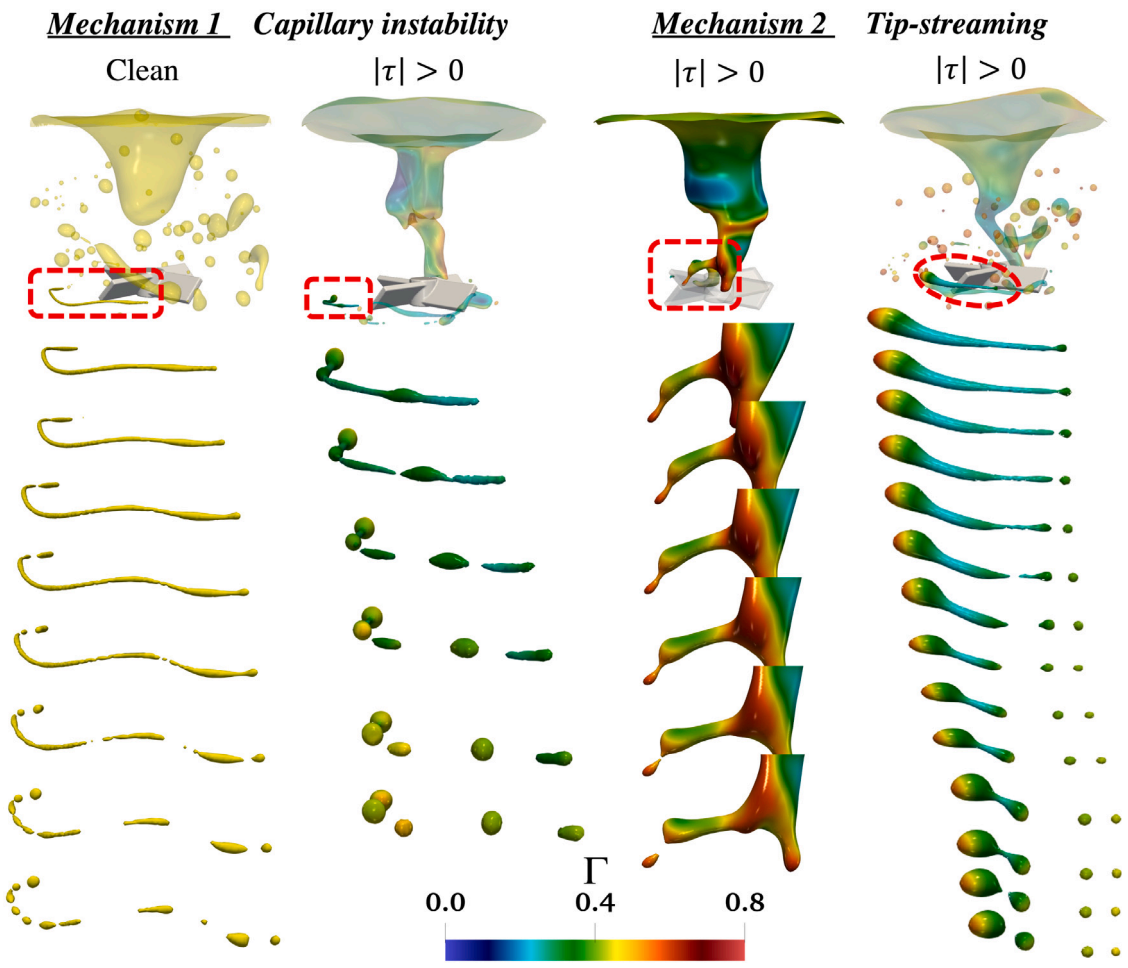

Fig. 6. Close-up visualisations of drop breakup mechanisms observed in surfactant-free system (left) at $t = 16.375 \times Rev.$, and surfactant-laden system I, at $t = 11.625, 12.375, 15.4 \times Rev.$ (from second left to right, respectively). The presented breakup events are via the capillary instability (left two columns), and surfactant-enhanced tip-streaming (right two columns). Two scenarios for tip-streaming are given, one initiated from the deforming interface and another from an elongated ligament. The surfactant-related parameters remain unchanged from Fig. 3.

Fig. 8-(*b*). In the first scenario, an emergent interfacial structure (circled in blue) formed from a coalescence event is elongated by the local flow and broken up again into several smaller drops. For the latter case, ligament production from the deforming interface (circled in red) eventually recurs given that adequate dispersed drops are merged back with the deforming interface.

3.3. Comparative statistics

3.3.1. Temporal evolution of dispersed entity number

In this part, the transient count of dispersed entities is tracked with the aim of quantifying the qualitative interfacial behaviours described in the last section. The four steps of liquid dispersion (see Section 3.1) can be related to three stages of the transient number profile of dispersed entities (which can be either a stretching ligament or an individual drop). Fig. 9-(*a*) presents the number profile along with the interfacial shape at the corresponding instants. Initially, *no dispersed drop* (Stage A, shown by dashed lines) formation is observed during the interface deformation (Step 1) since the interface is approaching the impeller. Then, the onset of ligament formation and subsequent breakup events (Steps 2 and 3) lead to a *dramatic increase* (Stage B, shown by solid lines) in the dispersed entity count. Finally, the cessation of impeller-interface contact (Step 4) gives rise to a *gentle fall-off* (Stage C, shown by dotted lines) as the dispersed drops tend to coalesce, or merge back with the overlying oil-phase (see close-up views in Fig. 9-(*a*)), while less or no new dispersed drops are formed.

The first distinction among the three cases is the compression of Stage A corresponding to a shortened duration of interface deformation. This can be explained with the accelerated interface deformation as demonstrated above. Furthermore, we noted here the distinguished increasing patterns at early Stage B for the three cases, as highlighted in the orange rectangle in Fig. 9-(*a*). The abrupt jump seen for the surfactant-free system comes naturally from the breakup events via capillary instability. By comparison, a mild increase appears prior to the steep rise for the surfactant-laden system I, which is the result of the early drop breakup events via tip-streaming from the deforming interface. Again, the early and more pronounced increase for the Marangoni-free system reflects the inhibiting effect of Marangoni stress on the drop deformation and therefore the breakup events.

During Stage B in Fig. 9-(*a*), an abrupt jump in the number of dispersed entities with a larger amplitude compared to the surfactant-free system is observed for the surfactant-laden system I. This is due to the onset of drop breakup events via both mechanisms stated above (capillary instability, and concurrently, tip-streaming). However, there exists a plateau following the dramatic increase ($t \approx 15 \times Rev.$), which indicates a deceleration of the dispersed phases formation. This can be related to the fact that tip-streaming, which generates drops intermittently, is promoted in surfactant-laden system I, and consequently, some ligaments generating drops via tip-streaming in that system break up into drops through capillary instability in surfactant-free system. Another interesting trend is the overlap between the two surfactant-laden cases, as highlighted in orange oval in Fig. 9-(*a*). As

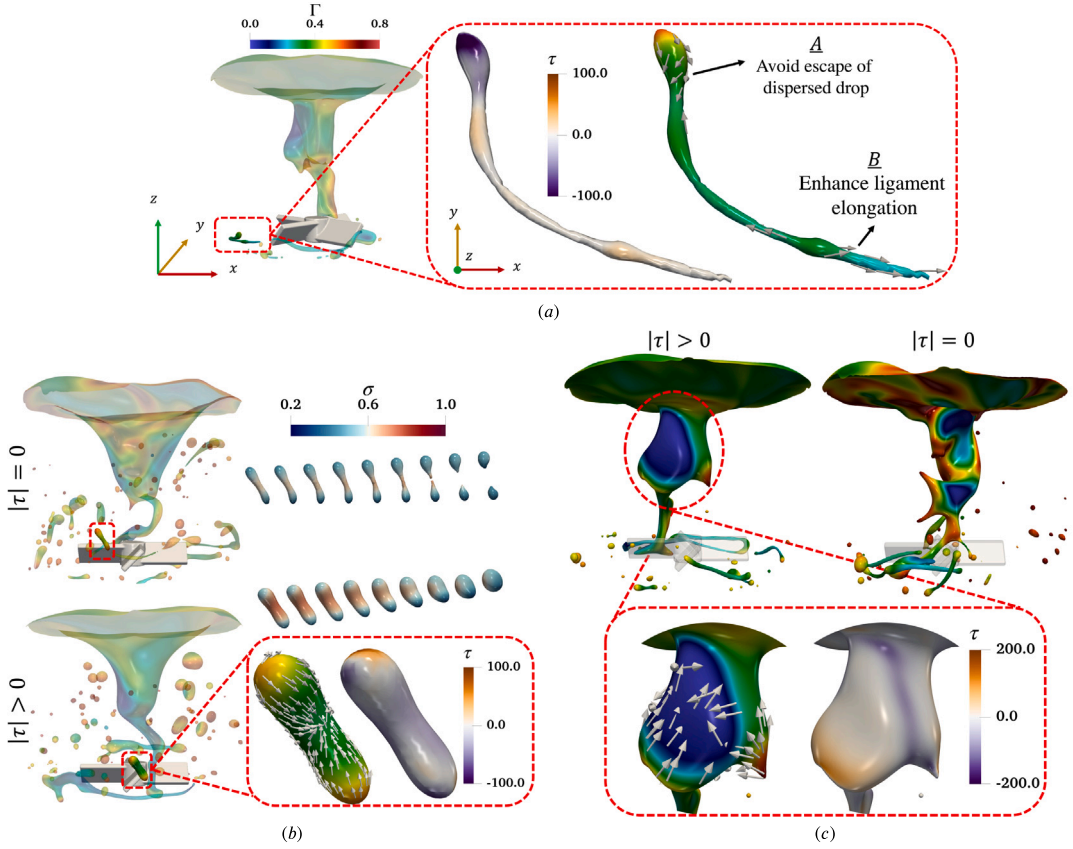

Fig. 7. Visualisations of Marangoni stresses under different scenarios: (a) ligament elongation prior to its fragmentation towards multiple drops; (b) drop deformation where the evolving drops are coloured using σ; and (c) evolution of the deforming interface shape. The insets consist of two identical interfacial states coloured in Γ and τ, respectively; the negative sign of τ represents its direction, and the grey arrows refers to the direction of Marangoni stresses. The surfactant-related parameters remain unchanged from Fig. 3.

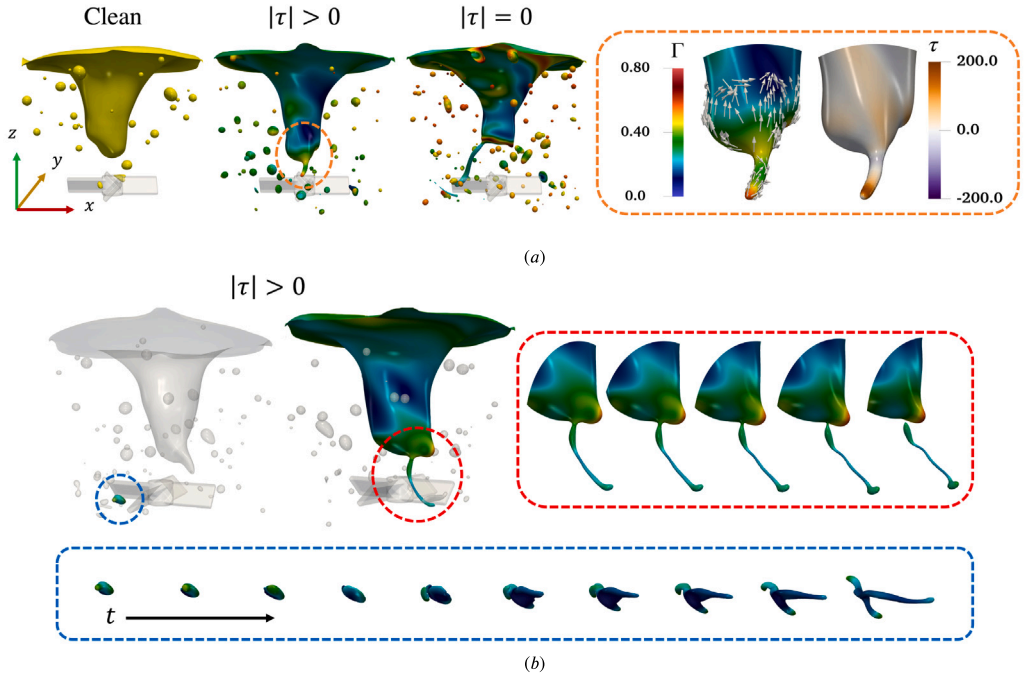

Fig. 8. (a) Interfacial shapes for the three studied systems at $t = 25 \times Rev.$, along with a similar inset showing the direction and magnitude of Marangoni stress as in Fig. 7; (b) exemplified interfacial evolution in the surfactant-laden I system presenting the different outcomes depending on dispersed drop behaviours. (i) Coalescence: ligament formation from consequent larger drop (circled in blue) elongation; (ii) merging back with the deforming interface: recurring ligament formation (circled in red) from the deforming interface. The surfactant-related parameters remain unchanged from Fig. 3.

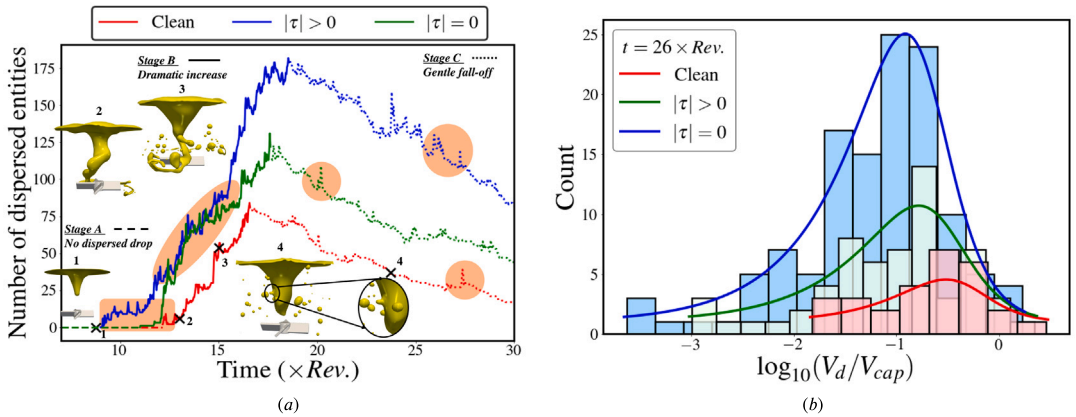

Fig. 9. (*a*) Temporal evolution of dispersed entities number for surfactant-free, surfactant-laden I, and surfactant-laden II systems for a time frame of $t = 7 - 30 \times Rev.$, along with the representative interfacial shapes corresponding to the four steps of liquid dispersion (at $t = 9, 13, 15, 23.5 \times Rev.$, exemplified by the surfactant-free case). This profile is divided into three stages: (A) no dispersed drop, (B) dramatic increase and (C) gentle fall-off, which are respectively shown by dashed, solid, and dotted lines; (*b*) fitted drop size distribution (Probability Density Function with respect to log-scale of normalised drop volume) at $t = 26 \times Rev.$ for the three cases. The surfactant-related parameters remain unchanged from Fig. 3.

demonstrated earlier, this reflects the fact that Marangoni stress aids the commencement of breakup events via capillary instability in the system with Marangoni stress turned on, and thus dispersed drops are generated rapidly enough to reach comparable amount to its counterpart for the Marangoni-free system, though a delayed appearance of the first dispersed drop is observed for the former system. Following the overlap, the drop count for the Marangoni-free system rises sharply until its peak is reached. This is due to the fact that a large amount of thin ligaments are formed simultaneously from the deforming interface, along with the drop production, which give rise to similarly increasing rate as in the case of a single breakup event via capillary instability. This provides additional evidence for the effect of the Marangoni stress on the interfacial dynamics and associated phenomena as reported in Section 3.2.2 and Fig. 7.

Another key aspect to highlight from Fig. 9-(*a*) is the appearance of humps in Stage C for all three cases (circled in orange), which can be indicative of the occurrence of dispersed interfacial structure formation, either from recurring ligament production or large coalesced drop fragmentation, as explored in Section 3.2.3. Eventually, the rate of drop formation and coalescence seems to stabilise somewhat, with a steady decline in the number of drops and smaller rates for the clean and Marangoni-free cases after $t = 28 \times Rev.$ compared to the onset of Stage C. From this point onward, the dynamics developing in the tank stagnate, reducing to sporadic coalescence and subsequent breakup chains as described in Section 3.2.3. For this reason, the simulations were terminated after this point.

Finally, the dispersed entities number at the instant where we terminated our simulations takes the following order: surfactant-free (17), surfactant-laden I (43), and surfactant-laden II (82) systems. This provides further indication of the surfactant effect on the liquid dispersion in the studied configuration as summarised below:

- The reduced interfacial tension promotes tip-streaming (or tip-dropping), which contributes to the formation of more dispersed drops in the surfactant-laden system I;
- The Marangoni stress, in general, acts to counteract and retard interfacial deformation and drop formation, which explains the larger dispersed phases number in its absence;
- Marangoni stress is found to encourage the breakup events via capillary instability, which is commonly occurs under general emulsion scenarios [62], and, to some extent, suppresses tip-streaming.

3.3.2. Drop size distribution

The dispersed entities number alone is not a representative metric of the effect of surfactant in the stirred mixer. Additionally, a drop size distribution analysis at $t = 26 \times Rev.$ is carried out for the three studied cases herein, as presented in Fig. 9-(*b*). The drop size in this context is defined as the volume of a dispersed entity, V_d, and is normalised by the volume of a spherical drop, V_{cap}, whose diameter corresponds to the capillary length scale, $\sqrt{\sigma_s(\rho_w - \rho_o)g}$.

The data structure has been evaluated using quantile–quantile (Q–Q) test and box plots, and the outliers (i.e., non-physical tiny drops and elongating large ligaments) are removed from the analysis. In the field of statistics, one commonly applies the Kolmogorov–Smirnov (K–S) test [75] and the Anderson–Darling (A–D) test [76] to examine the goodness of one population of data to fit one specific distribution; a non-parametric analysis of variance, for example, Kruskal–Wallis (K–W) test [77] is then used to contrast the distributions and the following Dunn's test [78,79] specifies the distinct sets of data. Following such procedure, the filtered data sets are fitted to a logistic distribution, satisfying both the K–S test and the A–D test with a significance level of 0.05. Furthermore, K–W test is conducted to contrast the distributions, where statistical significance is implied among the three data sets. More specifically, subsequent Dunn's test determines that the Marangoni-free system is distinct from (lower than) the other two systems, as far as their medians are concerned. This finding is consistent with the prior work [80] pointing out the manifold effects of surfactant on the average drop size, especially in mixing scenarios, as opposed to the assertion that the addition of surfactant simply reduces the interfacial tension, and therefore, the dispersed drop size. The deviation for the Marangoni-free data strengthens this statement indicating that the effect of surfactant on the drop size is not limited to lowering interfacial tension but also arises from the Marangoni stress, which plays a role in drop breakup mechanisms as demonstrated in previous sections.

Moreover, skewness and kurtosis are computed to examine the asymmetry (i.e., tail) of the distributions. First, negative skewness for all three cases signifies the left-tailed shape, which can be translated as all three cases exhibit an inclination to produce small drops. In regard to the magnitude (absolute value) of skewness, incremental skewness is obtained for the three cases following the order: surfactant-free (−0.23) < surfactant-laden I (−0.76) < surfactant-laden II (−1.01). In addition, the kurtosis indicates "heavier" tails for the same ordering, in other words, the surfactant-laden system II produces the largest amount of small drops, followed by the surfactant-laden I, and finally the surfactant-free system. This comparison leads to a similar conclusion as above: interfacial tension reduction promotes the production of smaller drops while the Marangoni stress acts to mitigate this effect.

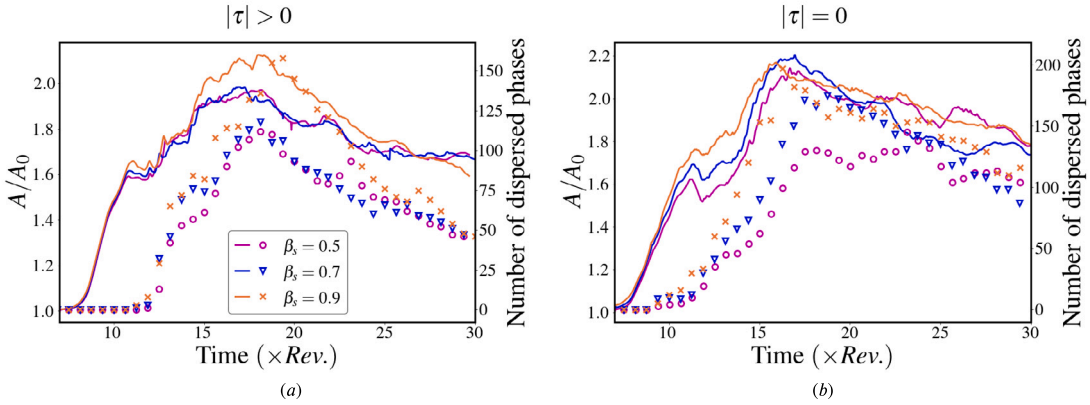

Fig. 10. A general quantitative insight into the mixing process for the systems with Marangoni stress turned on (*a*) and off (*b*), with regard to the evolution of interfacial area (lines) and dispersed entities count (symbols). Profiles of both metrics are displayed for varying surfactant elasticity numbers $\beta_s = 0.5, 0.7, 0.9$ during $t = 7 - 30 \times Rev.$. Except for the variations in β_s, the rest of the surfactant-related parameters remain unchanged from Fig. 3.

3.4. Effect of surfactant elasticity, β_s

Fig. 10-(*a*) and -(*b*) provide a quantitative insight into the mixing process in systems of varying elasticity numbers with respect to the evolution of the interfacial area (made dimensionless via the initial interfacial area, A_0) and dispersed phases count; (*a*) refers to the three cases with Marangoni stress turned on and (*b*) presents the Marangoni-free systems. It can be seen that prior to dispersed entity formation (i.e., Stage A defined in Section 3.3.1), a small change in interfacial area is seen for both Marangoni-free system and its counterpart in the presence of Marangoni stress. This is consistent with what we demonstrated in Section 3.2.1 that the elongational flow experienced by the deforming interface is so strong that the effect of increasing β_s (and therefore the modified interfacial tension and Maranogoni stress) is negligible during this step. After that, increasing β_s, which augments the sensitivity of interfacial tension to the surfactant concentration, generally promotes interface deformation and formation of dispersed entities (shown as incremental A/A_0 and entities count, respectively, in Fig. 10-(*b*)). However, these effects are only prominent prior to the fall-off (i.e., Stage C defined in Section 3.3.1). Following the onset of the fall-off, no distinguishable trend regarding either the interfacial area or dispersed entities count is seen for increasing β_s. Furthermore, in comparison with Fig. 10-(*a*), the presence of Marangoni stress mitigates the effects mentioned above. In other words, under realistic scenarios, increasing β_s from 0.5 to 0.7 leads to insignificant change in interfacial area and dispersed phases count. Instead, an obvious increase is seen in both metrics at $t = 15 - 25 \times Rev.$ for $\beta_s = 0.9$, the largest β_s studied herein.

To elucidate the observations highlighted above, Fig. 11 provides a comparison ($t = 9 \times Rev.$) among the three cases with Marangoni stress turned on in terms of surfactant-related properties on the interface. First, to gain a comprehensive insight into the surfactant property profile on the deforming interface, a quantity (for instance, the surfactant concentration Γ), is averaged over a horizontal slice of the interface. The averaged Γ, $\bar{\Gamma}$, on a sequence of horizontal slices, located at different heights of the interface, is then tracked. This gives Fig. 11-(*a*) where the markers refer to the $\bar{\Gamma}$ over the horizontal slice at the corresponding height, as demonstrated in the schematic inset. Similarly, Fig. 11-(*b*) plots the averaged interfacial tension and the strength of Marangoni stresses along the interface (vertically). From these figures, larger β_s results in lower interfacial tension, as expected, more uniform surfactant concentration (narrower range of $\bar{\Gamma}$), and larger Marangoni stress induced along the interface. As shown in the figure, the Marangoni stress on the waist of the interface (labelled as *a*, $\tilde{z} \approx 0.6$) is larger in magnitude augmenting deformation (negative, pointing downward); likewise, that induced in the lower part of the interface (labelled as *b*, $\tilde{z} \approx 0.1$) is stronger retarding deformation (positive, pointing upward). Meanwhile, the retarding force exceeds the augmenting one (take $\beta_s = 0.9$ as an example, $|\tau|_b \approx 32 > |\tau|_a \approx 9$). Hence, the sum of these effects is reflected as a negligible change in interfacial area (i.e., overlapping lines) as observed in Fig. 10.

The ensuing Fig. 11-(*c*) provides a comparison of the interfacial shapes for the three cases in the presence of Marangoni stress, illustrating the cause of the significant increase in interfacial area and dispersed entities count for $\beta_s = 0.9$. As shown in this figure, while the deforming interfaces in the other two cases start to retract and detach the impeller hub ($t = 17 \times Rev.$), the $\beta_s = 0.9$ case exhibits an interface in the shape of a tail extending to the vessel bottom. Several long stretching ligaments are also generated, which subsequently give way to multiple dispersed drops leading to a sharp increase in dispersed drop count. Such phenomenon lasts until $t = 18 \times Rev.$. On the other hand, this feature is missing for the Marangoni-free system. This provides further indication that one of the effects exerted by Marangoni stress is to encourage drop breakup via long ligament fragmentation driven by the capillary instability (see Section 3.2.2).

From above, the effect of β_s is best appreciated during the intermediate period of the mixing process, which corresponds to Steps 2 and 3 of the interfacial behaviours defined in Section 3.1. After the cessation of the interface-impeller contact, the effect of changing surfactant elasticity diminishes as displayed in the plots at the instant where we terminated our simulations; the cases associated with the three studied β_s produce similar interfacial area and dispersed entity count, for both the scenarios with Marangoni stress turned on and off. This implies that the effect of changing β_s is more pronounced on drop dispersion compared to coalescence. It should be noted, however, that due to the complex nature of the flow considered in the present work, larger computational resolution is required to recover the potential (and subtle) effect of surfactant on drop coalescence, which is beyond the discussion presented herein.

4. Conclusions

The current study has extended our previous work on numerical analysis regarding oil–water emulsification inside an un-baffled stirred vessel by accounting for the presence of soluble surfactant. We have contrasted the surfactant-free and surfactant-laden systems in terms of interfacial behaviours during mixing, transient number of dispersed phases, and drop size distribution at the instant where the simulations are terminated. Furthermore, our simulations allow us to turn off the Marangoni stress, which is evidently unachievable in experimental work. In this way, we have isolated the effects that arise from interfacial tension reduction and the Marangoni stress induced by surfactant concentration gradient. In general, the decrease in interfacial tension eases the interface deformation and drop formation in our system, promoting

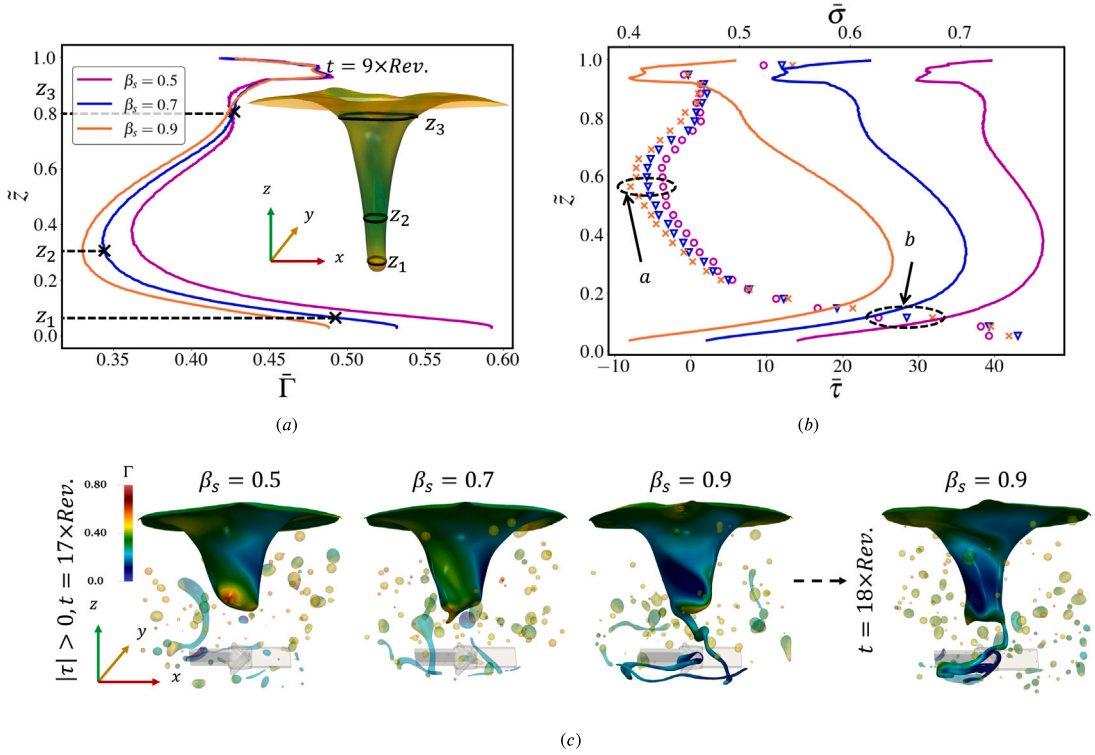

Fig. 11. The averaged surfactant properties along the interface at $t = 9 \times Rev.$, (*a*) the averaged surfactant concentration, $\bar{\Gamma}$; (*b*) the averaged interfacial tension ($\bar{\sigma}$, lines) and the averaged magnitude of Marangoni stresses ($\bar{\tau}$, symbols). The $\tilde{z}$ refers to the dimensionless height on the interface, scaled using the minimum position of the deforming interface as in Fig. 4; here, negative τ represents its direction pointing downward. (*c*) A comparison of the interfacial shapes for the three systems in the presence of Marangoni stress at $t = 17 \times Rev.$. Except for the β_s variations, the rest of the surfactant-related parameters remain unchanged from Fig. 3.

a second drop breakup mechanism, the tip-streaming/dropping, which is not observed in surfactant-free system. On the other hand, the role played by the Marangoni stresses is dependent on the local surfactant concentration distribution. In particular, it could either encourage breakup events via a capillary instability, or retard interfacial elongation and thereby drop production, especially via tip-streaming. From the perspective of drop size, the presence of surfactant exerts manifold effects such that lowering interfacial tension aids the production of smaller drops, while the Marangoni stress mitigates this influence.

In addition, a parametric study has been performed to address the effect of surfactant elasticity, β_s. We have demonstrated that increasing β_s facilitates interface deformation and thereby drop formation by decreasing the average interfacial tension. However, the presence of Marangoni stress counteracts these effects and leads to a sharp increase in both interfacial area and dispersed phases count for the largest β_s ($\beta_s = 0.9$) during $t = 15{-}20\times Rev.$, by encouraging the formation of long ligaments (and thereby subsequent drop production). Ultimately, the deviation vanishes at the instant we terminated the simulations where similar drop number and interfacial area are observed.

Throughout this work, we have provided a detailed insight into surfactant-laden interfacial dynamics within a practical operation unit, i.e., the stirred vessel. Though all the results are from a specific configuration, the physics we have discussed is generic to stirred mixers. Considering the flexibility provided by our simulations, our future work will address other surfactant properties including diffusion and sorption kinetics. We will also use our high-fidelity simulations to produce correlations of the drop size distributions with the dimensionless parameters that characterise our surfactant system.

Declaration of competing interest

The authors declare the following financial interests/personal relationships which may be considered as potential competing interests: O.K. Matar reports financial support was provided by Engineering and Physical Sciences Research Council. O.K. Matar reports a relationship with Engineering and Physical Sciences Research Council that includes: funding grants.

Data availability

Data will be made available on request.

Acknowledgements

This work is supported by the Engineering and Physical Sciences Research Council, United Kingdom, through the EPSRC MEMPHIS, United Kingdom (EP/K003976/1) and PREMIERE (EP/T000414/1) Programme Grants. O.K.M. acknowledges funding from PETRONAS and the Royal Academy of Engineering for a Research Chair in Multiphase Fluid Dynamics. We acknowledge HPC facilities provided by the Research Computing Service (RCS) of Imperial College London for the computing time. D.J. and J.C. acknowledge support through HPC/AI computing time at the Institut du Developpement et des Ressources en Informatique Scientifique (IDRIS) of the Centre National de la Recherche Scientifique (CNRS), coordinated by GENCI (Grand Equipement National de Calcul Intensif), France Grant 2023 A0142B06721.

Appendix A. Supplementary data

Supplementary material related to this article can be found online at https://doi.org/10.1016/j.cej.2023.144807. The SI section contains details of the validation studies carried out in which the predictions of the numerical procedure used to perform the computations in the present work are compared to experimental data.

References

[1] James M. Lee, Yee Soong, Effects of surfactants on the liquid-liquid dispersions in agitated vessels, Ind. Eng. Chem. Process Des. Dev. 24 (1) (1985) 118–121.
[2] Abraham Koshy, T.R. Das, R. Kumar, Effect of surfactants on drop breakage in turbulent liquid dispersions, Chem. Eng. Sci. 43 (3) (1988) 649–654.
[3] Eleni G. Chatzi, Costas J. Boutris, Costas Kiparissides, On-line monitoring of drop size distributions in agitated vessels. 1. Effects of temperature and impeller speed, Ind. Eng. Chem. Res. 30 (3) (1991) 536–543.
[4] Amer El-Hamouz, Effect of surfactant concentration and operating temperature on the drop size distribution of silicon oil water dispersion, J. Dispers. Sci. Technol. 28 (5) (2007) 797–804.
[5] E.H. Lucassen-Reynders, K.A. Kuijpers, The role of interfacial properties in emulsification, Colloids Surf. 65 (2–3) (1992) 175–184.
[6] Tanya Goloub, Robert J. Pugh, The role of the surfactant head group in the emulsification process: Single surfactant systems, J. Colloid Interface Sci. 257 (2) (2003) 337–343.
[7] F. Groeneweg, F. Van Dieren, W.G.M. Agterof, Droplet break-up in a stirred water-in-oil emulsion in the presence of emulsifiers, Colloids Surf. A 91 (1994) 207–214.
[8] Charles D. Eggleton, Tse-Min Tsai, Kathleen J. Stebe, Tip streaming from a drop in the presence of surfactants, Phys. Rev. Lett. 87 (4) (2001) 048302.
[9] V.P. Mishra, P. Kumar, J.B. Joshi, Flow generated by a disc turbine in aqueous solutions of polyacrylamide, Chem. Eng. J. 71 (1) (1998) 11–21.
[10] Kartik Arora, Radhakrishna Sureshkumar, Matthew P. Scheiner, Justin L. Piper, Surfactant-induced effects on turbulent swirling flows, Rheol. Acta 41 (1) (2002) 25–34.
[11] Paul Mavros, Alain Ricard, Catherine Xuereb, Joel Bertrand, A study of the effect of drag-reducing surfactants on flow patterns in stirred vessels, Chem. Eng. Res. Des. 89 (1) (2011) 94–106.
[12] Giuseppina Montante, Fabio Laurenzi, Alessandro Paglianti, Franco Magelli, A study on some effects of a drag-reducing agent on the performance of a stirred vessel, Chem. Eng. Res. Des. 89 (11) (2011) 2262–2267.
[13] Howard A. Stone, L. Gary Leal, The effects of surfactants on drop deformation and breakup, J. Fluid Mech. 220 (1990) 161–186.
[14] W.J. Milliken, Howard A. Stone, L.G. Leal, The effect of surfactant on the transient motion of Newtonian drops, Phys. Fluids A 5 (1) (1993) 69–79.
[15] Xiaofan Li, C. Pozrikidis, The effect of surfactants on drop deformation and on the rheology of dilute emulsions in Stokes flow, J. Fluid Mech. 341 (1997) 165–194.
[16] Charles D. Eggleton, Yashodhara P. Pawar, Kathleen J. Stebe, Insoluble surfactants on a drop in an extensional flow: a generalization of the stagnated surface limit to deforming interfaces, J. Fluid Mech. 385 (1999) 79–99.
[17] Ivan B. Bazhlekov, Patrick D. Anderson, Han E.H. Meijer, Numerical investigation of the effect of insoluble surfactants on drop deformation and breakup in simple shear flow, J. Colloid Interface Sci. 298 (1) (2006) 369–394.
[18] Kathleen Feigl, David Megias-Alguacil, Peter Fischer, Erich J. Windhab, Simulation and experiments of droplet deformation and orientation in simple shear flow with surfactants, Chem. Eng. Sci. 62 (12) (2007) 3242–3258.
[19] Giovanni Soligo, Alessio Roccon, Alfredo Soldati, Deformation of clean and surfactant-laden droplets in shear flow, Meccanica 55 (2) (2020) 371–386.
[20] William J. Milliken, L. Gary Leal, The influence of surfactant on the deformation and breakup of a viscous drop: The effect of surfactant solubility, J. Colloid Interface Sci. 166 (2) (1994) 275–285.
[21] Charles D. Eggleton, Kathleen J. Stebe, An adsorption–desorption-controlled surfactant on a deforming droplet, J. Colloid Interface Sci. 208 (1) (1998) 68–80.
[22] Fang Jin, Nivedita R. Gupta, Kathleen J. Stebe, The detachment of a viscous drop in a viscous solution in the presence of a soluble surfactant, Phys. Fluids 18 (2) (2006) 022103.
[23] Fang Jin, Kathleen J. Stebe, The effects of a diffusion controlled surfactant on a viscous drop injected into a viscous medium, Phys. Fluids 19 (11) (2007) 112103.
[24] B.J. Briscoe, C.J. Lawrence, W.G.P. Mietus, A review of immiscible fluid mixing, Adv. Colloid Interface Sci. 81 (1) (1999) 1–17.
[25] Peter Fischer, Philipp Erni, Emulsion drops in external flow fields—the role of liquid interfaces, Curr. Opin. Colloid Interface Sci. 12 (4–5) (2007) 196–205.
[26] Giovanni Soligo, Alessio Roccon, Alfredo Soldati, Breakage, coalescence and size distribution of surfactant-laden droplets in turbulent flow, J. Fluid Mech. 881 (2019) 244–282.
[27] Giovanni Soligo, Alessio Roccon, Alfredo Soldati, Effect of surfactant-laden droplets on turbulent flow topology, Phys. Rev. Fluids 5 (7) (2020) 073606.
[28] Anthony E. Perry, Min S. Chong, A description of eddying motions and flow patterns using critical-point concepts, Annu. Rev. Fluid Mech. 19 (1) (1987) 125–155.
[29] A. Busciglio, F. Grisafi, F. Scargiali, A. Brucato, Mixing dynamics in uncovered unbaffled stirred tanks, Chem. Eng. J. 254 (2014) 210–219.
[30] A. Busciglio, F. Scargiali, F. Grisafi, A. Brucato, Oscillation dynamics of free vortex surface in uncovered unbaffled stirred vessels, Chem. Eng. J. 285 (2016) 477–486.
[31] Seungwon Shin, Jalel Chergui, Damir Juric, Lyes Kahouadji, Omar K. Matar, Richard V. Craster, A hybrid interface tracking–level set technique for multiphase flow with soluble surfactant, J. Comput. Phys. 359 (2018) 409–435.
[32] C.R. Constante-Amores, A. Batchvarov, L. Kahouadji, S. Shin, J. Chergui, Damir Juric, O.K. Matar, Role of surfactant-induced Marangoni stresses in drop-interface coalescence, J. Fluid Mech. 925 (2021).
[33] Cristian R. Constante-Amores, Lyes Kahouadji, Assen Batchvarov, Seungwon Shin, Jalel Chergui, Damir Juric, Omar K. Matar, Dynamics of a surfactant-laden bubble bursting through an interface, J. Fluid Mech. 911 (2021).
[34] Fuyue Liang, Lyes Kahouadji, Juan Pablo Valdes, Seungwon Shin, Jalel Chergui, Damir Juric, Omar K. Matar, Numerical study of oil-water emulsion formation in stirred vessels: effect of impeller speed, Flow 2 (2022) E34.
[35] Seungwon Shin, Jalel Chergui, Damir Juric, A solver for massively parallel direct numerical simulation of three-dimensional multiphase flows, J. Mech. Sci. Technol. 31 (4) (2017) 1739–1751.
[36] Douglas Keith Lilly, On the application of the eddy viscosity concept in the inertial sub-range of turbulence, NCAR Manuscr. 123 (1966).
[37] Douglas K. Lilly, The representation of small-scale turbulence in numerical simulation experiments, IBM Form (1967) 195–210.
[38] James W. Deardorff, A numerical study of three-dimensional turbulent channel flow at large Reynolds numbers, J. Fluid Mech. 41 (2) (1970) 453–480.
[39] Oden J. McMillan, Joel H. Ferziger, Direct testing of subgrid-scale models, AIAA J. 17 (12) (1979) 1340–1346.
[40] Stephen B. Pope, Ten questions concerning the large-eddy simulation of turbulent flows, New J. Phys. 6 (1) (2004) 35.
[41] Johan Meyers, Pierre Sagaut, On the model coefficients for the standard and the variational multi-scale Smagorinsky model, J. Fluid Mech. 569 (2006) 287–319.
[42] Lyes Kahouadji, Fuyue Liang, Juan P. Valdes, Seungwon Shin, Jalel Chergui, Damir Juric, Richard V. Craster, Omar K. Matar, The transition to aeration in turbulent two-phase mixing in stirred vessels, Flow 2 (2022) E30.
[43] Harishankar Manikantan, Todd M. Squires, Surfactant dynamics: hidden variables controlling fluid flows, J. Fluid Mech. 892 (2020) P1.
[44] Chien-Hsiang Chang, Elias I. Franses, Adsorption dynamics of surfactants at the air/water interface: a critical review of mathematical models, data, and mechanisms, Colloids Surf. A 100 (1995) 1–45.
[45] Assen Batchvarov, Lyes Kahouadji, Mirco Magnini, Cristian R. Constante-Amores, S. Shin, J. Chergui, D. Juric, R.V. Craster, Omar K. Matar, Effect of surfactant on elongated bubbles in capillary tubes at high Reynolds number, Phys. Rev. Fluids 5 (9) (2020) 093605.
[46] Assen Batchvarov, Lyes Kahouadji, Cristian R. Constante-Amores, Gabriel F. Norões Gonçalve, S. Shin, J. Chergui, D. Juric, R.V. Craster, Omar K. Matar, Three-dimensional dynamics of falling films in the presence of insoluble surfactants, J. Fluid Mech. 906 (2021) A16.
[47] C.R. Constante-Amores, L. Kahouadji, A. Batchvarov, S. Shin, J. Chergui, Damir Juric, O.K. Matar, Dynamics of retracting surfactant-laden ligaments at intermediate Ohnesorge number, Phys. Rev. Fluids 5 (2020).
[48] C.R. Constante-Amores, T. Abadie, L. Kahouadji, S. Shin, J. Chergui, D. Juric, A.A. Castrejon-Pita, O.K. Matar, Direct numerical simulations of turbulent jets: vortex–interface–surfactant interactions, J. Fluid Mech. 955 (2023) A42.
[49] J. Mohd-Yusof, Combined immersed-boundary / B-spline methods for simulations of flow in complex geometries, in: Center for Turbulence Research Annual Research Briefs, 1997, pp. 317–327.
[50] E.A. Fadlun, R. Verzicco, P. Orlandi, J. Mohd-Yusof, Combined immersed-boundary finite-difference methods for three-dimensional complex flow simulations, J. Comput. Phys. 161 (2000) 35–60.
[51] A.W. Russell, L. Kahouadji, K. Mirpuri, A. Quarmby, P.M. Piccione, O.K. Matar, P.F. Luckham, C.N. Markides, Mixing viscoplastic fluids in stirred vessels over multiple scales: A combined experimental and CFD approach, Chem. Eng. Sci. 208 (2019) 115129.
[52] Rennan Pan, John Green, Charles Maldarelli, Theory and experiment on the measurement of kinetic rate constants for surfactant exchange at an air/water interface, J. Colloid Interface Sci. 205 (2) (1998) 213–230.
[53] Chengdi Dong, Ching-Tien Hsu, Chin-Yuan Chiu, Shi-Yow Lin, A study on surfactant adsorption kinetics: Effect of bulk concentration on the limiting adsorption rate constant, Langmuir 16 (10) (2000) 4573–4580.
[54] Yunfei He, Pavel Yazhgur, Anniina Salonen, Dominique Langevin, Adsorption–desorption kinetics of surfactants at liquid surfaces, Adv. Colloid Interface Sci. 222 (2015) 377–384.
[55] Andrei A. Levchenko, Brian P. Argo, Ruxandra Vidu, Raisa V. Talroze, Pieter Stroeve, Kinetics of sodium dodecyl sulfate adsorption on and desorption from self-assembled monolayers measured by surface plasmon resonance, Langmuir 18 (22) (2002) 8464–8471.
[56] Pritish M. Kamat, Brayden W. Wagoner, Sumeet S. Thete, Osman A. Basaran, Role of Marangoni stress during breakup of surfactant-covered liquid threads: reduced rates of thinning and microthread cascades, Phys. Rev. Fluids 3 (4) (2018) 043602.
[57] J. Ratulowski, H.-C. Chang, Marangoni effects of trace impurities on the motion of long gas bubbles in capillaries, J. Fluid Mech. 210 (1990) 303–328.
[58] Vladislav Hančil, Vladimír Rod, Break-up of a drop in a stirred tank, Chem. Eng. Process.: Process Intensif. 23 (3) (1988) 189–193.
[59] Nannan Liu, Wei Wang, Yunya Tian, Changchun Wu, Jing Gong, Experimental and numerical study for drop size distribution in oil-water dispersions with nonionic surfactant Tween 80, Exp. Therm Fluid Sci. 89 (2017) 153–165.

[60] Hermann Schlichting, Joseph Kestin, Boundary Layer Theory, Vol. 121, Springer, 1961.
[61] Edward L. Paul, Victor A. Atiemo-Obeng, Suzanne M. Kresta, Handbook of Industrial Mixing, Wiley Online Library, 2004.
[62] J.M.H. Janssen, H.E.H. Meijer, Droplet breakup mechanisms: Stepwise equilibrium versus transient dispersion, J. Rheol. 37 (4) (1993) 597–608.
[63] J.J.M. Janssen, A. Boon, W.G.M. Agterof, Influence of dynamic interfacial properties on droplet breakup in simple shear flow, AIChE J. 40 (12) (1994) 1929–1939.
[64] H. Wu, G.K. Patterson, Laser-Doppler measurements of turbulent-flow parameters in a stirred mixer, Chem. Eng. Sci. 44 (10) (1989) 2207–2221.
[65] Liangchao Li, Jiajun Wang, Lianfang Feng, Xueping Gu, Computational fluid dynamics simulation of hydrodynamics in an uncovered unbaffled tank agitated by pitched blade turbines, Korean J. Chem. Eng. 34 (11) (2017) 2811–2822.
[66] Ying Fan, Jiao Sun, Jie Jin, Hui Zhang, Wenyi Chen, The effect of baffle on flow structures and dynamics stirred by pitch blade turbine, Chem. Eng. Res. Des. 168 (2021) 227–238.
[67] Julius O. Hinze, Fundamentals of the hydrodynamic mechanism of splitting in dispersion processes, AIChE J. 1 (3) (1955) 289–295.
[68] Andreas Håkansson, Peyman Olad, Fredrik Innings, Identification and mapping of three distinct breakup morphologies in the turbulent inertial regime of emulsification—Effect of Weber number and viscosity ratio, Processes 10 (11) (2022) 2204.
[69] Harold P. Grace, Dispersion phenomena in high viscosity immiscible fluid systems and application of static mixers as dispersion devices in such systems, Chem. Eng. Commun. 14 (3–6) (1982) 225–277.
[70] Hong Bai Chin, Chang Dae Han, Studies on droplet deformation and breakup. II. Breakup of a droplet in nonuniform shear flow, J. Rheol. 24 (1) (1980) 1–37.
[71] Ronald Laymon, Newton's bucket experiment, J. Hist. Philos. 16 (4) (1978) 399–413.
[72] Thomas R.N. Jansson, Martin P. Haspang, Kåre H. Jensen, Pascal Hersen, Tomas Bohr, Polygons on a rotating fluid surface, Phys. Rev. Lett. 96 (17) (2006) 174502.
[73] Lyes Kahouadji, L. Martin Witkowski, Free surface due to a flow driven by a rotating disk inside a vertical cylindrical tank: axisymmetric configuration, Phys. Fluids 26 (7) (2014) 072105.
[74] Georgios H. Vatistas, A note on liquid vortex sloshing and Kelvin's equilibria, J. Fluid Mech. 217 (1990) 241–248.
[75] Frank J. Massey Jr., The Kolmogorov-Smirnov test for goodness of fit, J. Amer. Statist. Assoc. 46 (253) (1951) 68–78.
[76] Theodore W. Anderson, Donald A. Darling, A test of goodness of fit, J. Amer. Statist. Assoc. 49 (268) (1954) 765–769.
[77] William H. Kruskal, W. Allen Wallis, Use of ranks in one-criterion variance analysis, J. Amer. Statist. Assoc. 47 (260) (1952) 583–621.
[78] Olive Jean Dunn, Multiple comparisons among means, J. Amer. Statist. Assoc. 56 (293) (1961) 52–64.
[79] Olive Jean Dunn, Multiple comparisons using rank sums, Technometrics 6 (3) (1964) 241–252.
[80] Gustavo A. Padron, Effect of Surfactants on Drop Size Distributions in a Batch, Rotor-Stator Mixer (Ph.D. thesis), 2004.